High-resolution heat transfer measurements on a rotating turbine endwall with infrared thermography

T Ostrowski*[ID] and H-P Schiffer[ID]

Institute of Gas Turbines and Aerospace Propulsion, Technische Universität Darmstadt,
Otto-Berndt-Straße 2, 64287 Darmstadt, Germany

E-mail: ostrowski@glr.tu-darmstadt.de

CrossMark

Abstract

Computational thermo-fluid dynamics in the field of turbo machinery research tend to account for transient interaction mechanisms to predict the convective heat transfer within the hot gas path. In this context, the rotor hub side endwall region of the high pressure turbine depicts an object of interest as the near wall flow field may be dominated by rotating flow structures emerging from the disc space cavities. The validation of the applied numerical tools rely on experimental heat transfer setups reproducing such transient boundary conditions. This paper describes an experimental approach to quantify the heat transfer coefficient and the adiabatic wall temperature on the rotating endwall of a large scale test turbine. The wall heat flux distribution in a thin film isolator coated to a well conducting support structure is quantified for a series of quasi-isothermal boundary conditions. A high-resolution infrared camera is used to capture triggered thermograms of the rotating surface. Distributed thermocouples in the base body serve as reference points for camera calibration and to deduce the temperature distribution at the interface to the isolator. The calibration is *in-situ* and includes the pixel-wise quantification of uncertainties in the surface temperatures. An advanced linear fit approach is applied to derive the unknown adiabatic quantities and their uncertainties. For the examined operating point with a rim seal purge flow rate of 1% the random part of the relative measurement uncertainty is clearly below 10% for the heat transfer coefficient and below 5% for the adiabatic wall temperature. As the evaluation algorithm is designed to consider covariances between the thermocouple and infrared readings, the surface wall heat flux can be evaluated for every single infrared image.

Keywords: infrared thermography, moving objects, axial turbine, heat transfer coefficient,
film cooling effectiveness, linear regression, combined uncertainty

(Some figures may appear in colour only in the online journal)

---

* Author to whom any correspondence should be addressed.

1. Introduction

In the field of turbo-machinery research and development the quantification of thermal loads within the high pressure turbine section is crucial for the design of next generation aircraft engines and stationary gas turbines. Coming from the combustor section the hot exhaust gas passes the first high pressure stator vanes to subsequently drive the first rotor. Besides the thermal load the rotor hub side endwall region is highly stressed by centrifugal forces. The rotating hub is naturally separated from the stationary structure by gaps and cavities. To avoid the ingestion of hot gas, the gap is constantly sealed with comparably cold secondary air often termed as *rim seal purge flow*. The interaction between purge and main flow strongly influences the temperature and velocity distribution within the downstream rotor passage, mainly in the vicinity of the hub side endwall.

The mixing process is naturally influenced by the flow-guiding geometry of the seal itself. Basic experimental investigations of the aero-thermal effect of purge flow to the rotor endwall regime were made on linear cascades. Popovic *et al* [1] and Lynch and Thole [2] have quantified the negative effect of increasing purge flow rates on stage efficiency and for the same configurations its influence on overall and local endwall heat transfer. Another stationary high-resolution heat transfer study is presented in Laveau *et al* [3]. Laveau's concept to simultaneously derive the heat transfer coefficient and the adiabatic wall temperature served as one reference for the study presented in Werschnik *et al* [4]. The work of Schuler [5] represents a comprehensive experimental aero-thermal study on the effect of rim seal purge flow to the hub side endwall region. Schuler's linear cascade results show the benefit to accompany heat transfer studies with the experimental investigation of the near wall flow field.

In the real engine however the mixing process is furthermore influenced by the unsteady interaction between the stationary vane flow and the rotating flow field of the blade rows. Within the last two decades, the unsteady effect of this stator-rotor interaction to the rim seal flow structures came more and more into focus. In their unsteady CFD-study Boudet *et al* [6] provided an early evidence of low frequency pressure fluctuations, both inside the rim seal and in the hub side region of the main flow. Within their extensive time-resolved experimental aerodynamic study Schüpbach *et al* [7] confirmed the existence of subharmonic fluctuations. A spectral analysis of the raw-voltage of a *Fast Response Aerodynamic Probe* in the rotor exit plane showed increased amplitudes of the subharmonics within the hub side passage vortex. This is an early experimental evidence, that cavity vortex structures may influence the near wall flow field throughout the whole down-stream rotor passage. In Chilla *et al* [8] detailed CFD-calculations show a cavity vortex shedding into the hub side passage flow structure. Confirmed by more recent studies by Beard *et al* [9] the unsteady CFD results show cavity vortex structures with non periodic blade passing frequencies.

In an experimental and numerical study Schädler *et al* [10] investigated the radial migration of hub cavity modes into the main annulus flow field. The presented time-resolved measurements and the full annular simulations show the importance of including the potential low-frequency hub cavity modes into the design process of the turbine section. Within the work of Horwood *et al* [11] a numerical URANS-setup on a sector model of the 1.5-stage turbine test facility again led to low-pressure structures rotating with a fraction of the disc speed. Again, a detailed look into the resulting flow field showed the migration of those structures deep into the lower part of the passage flow. The study is continued by Hualca *et al* [12] and the influence of the flow guiding structures within the main flow path is analyzed.

As the unsteadiness of the cavity vortex structures evidentially influences the near endwall flow field in the downstream rotor passage, its effect on the heat transfer is not negligible. In an early experimental and numerical study Abhari *et al* [13] showed the general influence of unsteady stator-rotor interaction to the heat transfer in the rotating frame of reference. Even though the study was not accounting for any low-frequency modes arising from a rim seal purge flow, the importance of realizing a rotating and thereby unsteady setup is shown to be crucial for the prediction of heat transfer in a turbine rotor, both experimentally and numerically. The work of Blair *et al* [14] represents one of the early studies with spatially resolved heat transfer quantities in a large scale rotating rig environment. The experimental approach is based on distributed thermocouples in the rotating frame of reference and a liquid crystal technique to increase the spatial resolution.

Laveau *et al* [15] successfully adopted the infrared based measurement concept, as developed for the linear cascade setup [3], to the endwall in the first vane passage of a full annular rotating turbine facility. Subsequently, the measurement concept was changed to an iso-energetic approach and established for the experimental determination of heat transfer quantities in the rotating frame of reference. The experimental setup was first presented in Gazzini *et al* [16] and the sensitivity and uncertainty of the method was generally judged as adequate to meet the requirements in aero-thermal gas turbine studies with the focus on the rotor hub side region. A first technical study on the effect of different rim seal injection rates on the rotor endwall is documented in Gazzini *et al* [17] and continued by Hänni *et al* [18].

As published in Werschnik *et al* [19], the heat transfer measurement technique as applied in the linear cascade [4] was adopted to the first stator endwall of the *Large Scale Turbine Rig* (LSTR), a large scale low Mach number turbine test facility operated by the *Institute of Gas Turbines and Aerospace Propulsion* at *Technische Universität Darmstadt*. For the work presented in this paper, the aforementioned setup was adapted and enhanced to be applicable to the rotor hub side endwall at the LSTR.

After the clarification of the measurement principle, this paper first describes the practical implementation into the rotor structure of the rig. The data reduction algorithm is presented with a focus on the *in-situ* calibration procedure and the incorporated frame-wise calculation of the local wall heat flux.

An advanced linear fit approach is applied to derive the adiabatic quantities and their random measurement uncertainties. To introduce the application-oriented capability of the method, heat transfer results are shown for two different rim seal purge flow rates.

2. Methods and experimental setup

2.1. Measurement principle

The heat transfer coefficient h is widely used to correlate a driving temperature difference and the resulting specific heat flux q_W at a solid to fluid interface. Assuming that T_F and T_W are well chosen definitions of the fluid and wall temperature, this leads to the general expression of the convective heat transfer coefficient:

$$q_W = h\,(T_W - T_F) \;\rightarrow\; h = \frac{q_W}{T_W - T_F}. \tag{1}$$

The definition of the specific heat flux is on the other hand directly connected to the thermal conductivity of the fluid λ_F and the local temperature gradient at the interface of fluid to wall and is described by the equation for heat conduction, well known as the fundamental law of Fourier. Using the law of Fourier to substitute the specific heat flux in equation (1), the expression for the heat transfer coefficient may be rewritten as:

$$q_W = -\lambda_F \left(\frac{\partial T}{\partial y}\right)_W \;\rightarrow\; h = -\lambda_F \frac{\left(\frac{\partial T}{\partial y}\right)_W}{T_W - T_F}. \tag{2}$$

For most technical applications the experimental determination of the aforementioned temperature gradient in the direct vicinity of the wall is hard to realize. One common way to overcome this difficulty is to quantify the heat flux into the solid. Two approaches are generally distinguished: first the so called iso-energetic methods, where a boundary condition with a homogeneous heat flux is preferred. Second, an iso-thermal boundary condition, where the temperature distribution is assumed to be homogenous. In both cases the local heat flux together with the wall temperature and an appropriate reference for the fluid temperature allows the calculation in the form of equation (1).

The presented measurement principle is based on the direct determination of the local heat flux quantified in a thin layer of low conductive material, subsequently termed as the insulator. The thermal boundary condition may be regarded as quasi isothermal since the temperature of the body underneath the insulating layer is thermally controlled to reach a close to homogenous distribution. Assuming the heat flux to be normal to the insulating layer it equates to the local q_W as specified in equations (1) and (2). For the heat flux determination the temperature distributions on both sides of the insulator have to be determined. In the following, T_W is the temperature of the fluid facing surface, T_C is the temperature at the interface of carrier and insulation and q_I the corresponding specific heat flux. The
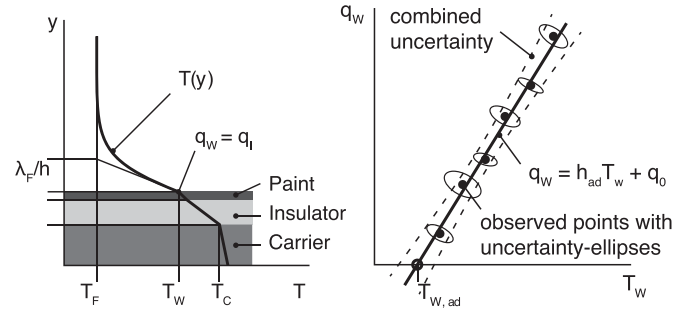

Figure 1. Measurement principle - The local specific heat flux q_W is quantified in a thin insulating layer. A series of temperature levels then lead to pairs of q_W and T_W allowing a linear fit procedure to derive the two unknown adiabatic quantities.

constant of proportionality is the thermal transmission coefficient k.

$$q_W = -k\,(T_W - T_C) \tag{3}$$

k describes the composition of the coating, which is built up of two layers. The insulator itself is finished with a highly emitting paint. For a 1D heat conduction problem in a multi-layer wall the effective k accounts for the series connection. Indexing the insulator and paint with I and P respectively, the effective k is determined as

$$1/k = \sum s_i/\lambda_i \;\rightarrow\; k = \frac{\lambda_I \lambda_P}{s_I \lambda_P + s_P \lambda_I} \tag{4}$$

where λ_i are the respective thermal conductivities and s_i the local wall thicknesses. The composition of the wall including a sketch of the temperature profile is depicted in figure 1(a).

For the expression of the heat transfer coefficient, compare equation (1), this leads to:

$$h = \frac{q_W}{T_W - T_F} = -k\frac{T_W - T_C}{T_W - T_F}. \tag{5}$$

From equation (5) the measurement procedure to experimentally determine the local heat transfer coefficient is obvious. With knowledge of the transmission k and the temperature difference over the insulating layer, the local specific heat flux is quantified and put into proportion with an appropriate driving temperature difference.

For simple heat transfer configurations the reference temperature of the fluid T_F may be an average temperature of the bulk mass flow. In film cooled regions however, the near wall temperature distribution will show high gradients and it is common to reference h to the local adiabatic wall temperature $T_{W,ad}$. The fact that the adiabatic assumption represents the local effective driving temperature, the definition is more general and enables the comparison of different configurations. The concept and basic principle of using the local adiabatic wall temperature $T_{W,ad}$ as a reference for the heat transfer in convective processes is well described by Moffat *et al* [20].

For the experimental determination of the adiabatic heat transfer coefficient at least two thermal boundary conditions

are necessary. Basically two approaches are possible to experimentally set up the two conditions. First, the adiabatic wall is set up directly by a highly insulated structure within the area of interest (AOI) together with a boundary with an enforced heat flux q_W between wall and boundary is created. Second, the adiabatic wall is not directly investigated but is somehow inter or extrapolated from a series of non adiabatic boundary conditions. This approach, however, is based on the assumption that the convective process is a linear function of the thermal boundary condition. This demand is hardly consistent to the governing energy equation. Even if the flow field as well as the temperature distribution in the fluid domain is kept constant, the fluids property values will change at the fluid to wall interface. But, if the temperature dependency of the fluid property is negligible and the external flow is kept constant, one may identify the adiabatic wall temperature using a straight line fit approach in the T_W-q_W coordinate system. A detailed explanation on this hypothesis can be found in Gritsch *et al* [21]. With the definitions made so far, the linear dependency between q_W and T_W is described with the following straight line expression:

$$q_W(T_W) = h_{ad} T_W + q_0. \tag{6}$$

As obvious, the slope equals to the adiabatic heat transfer coefficient and the adiabatic wall temperature is equated straight forward as the T_W-intercept as:

$$T_{W,ad} = -\frac{q_0}{h_{ad}}. \tag{7}$$

The robustness of the derived straight line is the basic principal to achieve high quality results. To reduce uncertainties in the two coefficients, multiple observed points may be experimentally surveyed leading to the necessity of a best-fit procedure. For the method presented in this paper, an advanced fitting approach is chosen. Besides the quality of the fit itself the method must also enable the quantification of uncertainties of the derived coefficients. As presented in detail in section 4, the implemented fit-procedure accounts for uncertainties in and correlations between both measures q_W and T_W. The implemented linear fit approach is illustrated in figure 1(b). Each observed point is sketched as the average together with it is corresponding uncertainty-ellipse built from both, the individual uncertainties in T_W and q_W and their covariances. The combined uncertainty of both coefficients finally allow the determination of the variance at the T_W-intercept as indicated with the dashed lines.

2.2. Experimental approach

The test section of the rig carries a large scale model of the first 1.5-stages of a shroud-less high pressure axial turbine. The test turbine is embedded into a temperature and pressure controlled closed loop wind tunnel environment. An independent secondary air system provides various supply lines for cooling and sealing air investigations, with individually controllable temperatures and mass flows. The rig environment and the measurement section are depicted in figure 2. For the presented heat
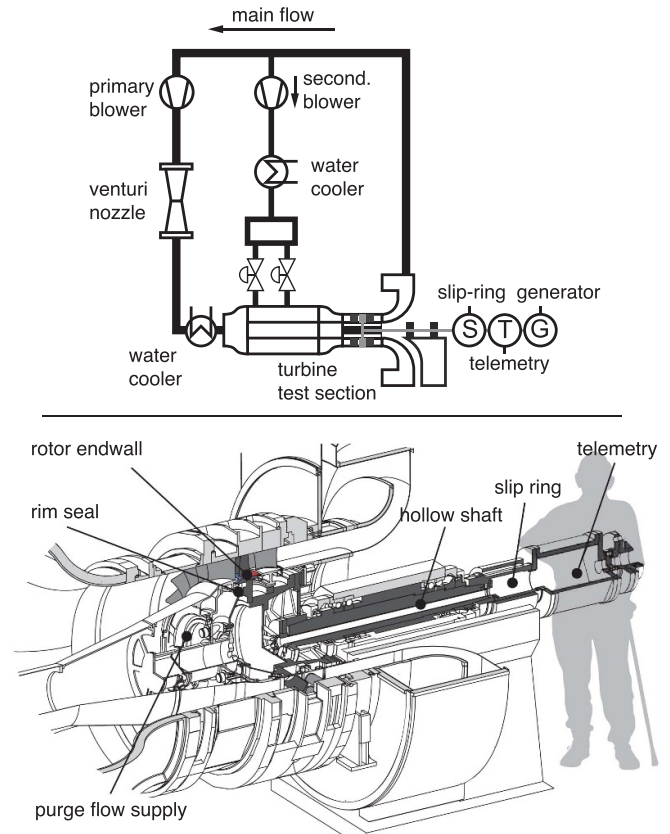

Figure 2. Flow chart of the turbine test facility and a 3D sectional view of the test turbine.

transfer study the low Mach number test rig is operated with a constant turbine inlet temperature of 313 K. To allow the quantification of the local adiabatic film cooling effectiveness a temperature difference between cooling and main flow is mandatory. With respect to the cooling capacity of the secondary air system the rim seal purge flow is controlled to 323 K. The total mass flow and the rotational speed are set to 10.33 kg s^{-1} and 1000 min^{-1}, respectively. All operating parameters are specific for the tested turbine and lead to an engine-realistic Reynolds number and a turbine specific flow coefficient at the rotor inlet. Further information on the operating parameters, their uncertainties, rig stability and repeatability are summarized in Eitenmüller *et al* [22].

The investigated rim seal geometry is classified as overlapping and depicted enlarged in the sectional view in figure 3. The circumferential speed of the hub is 45 m s^{-1}. Accounting for the blade height and the turbine casing design with its optical access, the distance between AOI and the objective lens is in the range of 200 mm.

The thermograms of the surface are captured with the infrared camera FLIR X654OSC. The camera with an InSb sensor has a spectral range of 1.5–5.5 µm and a resolution of 640 × 512 pixels. The average spatial resolution of the AOI is 5.6 px mm^{-1} leading to approximately 540 px for one rotor pitch. For the observation of moving objects, the choice of the integration time is often a trade-off between signal strength
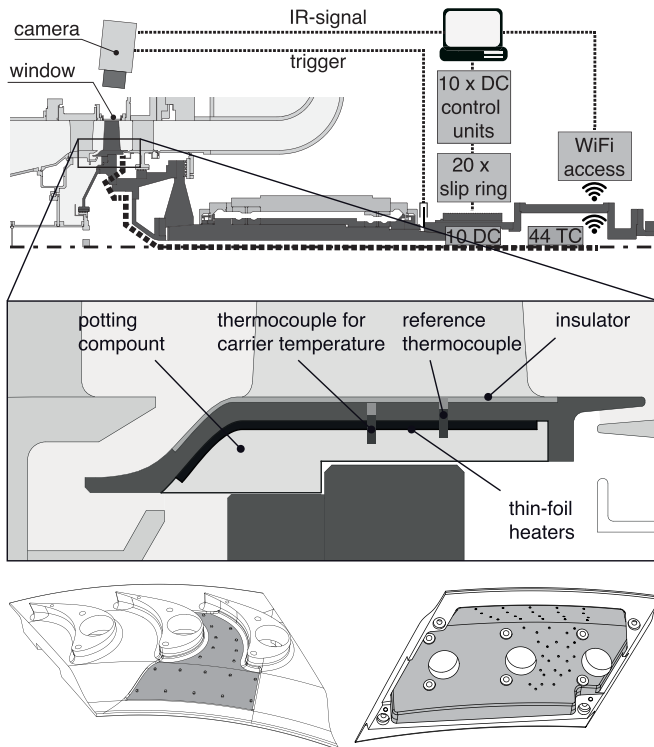
Figure 3. The heat transfer measurement setup. An instrumented measurement inlay is embedded into the rotating hub structure. Thermograms are captured with a triggered infrared camera.
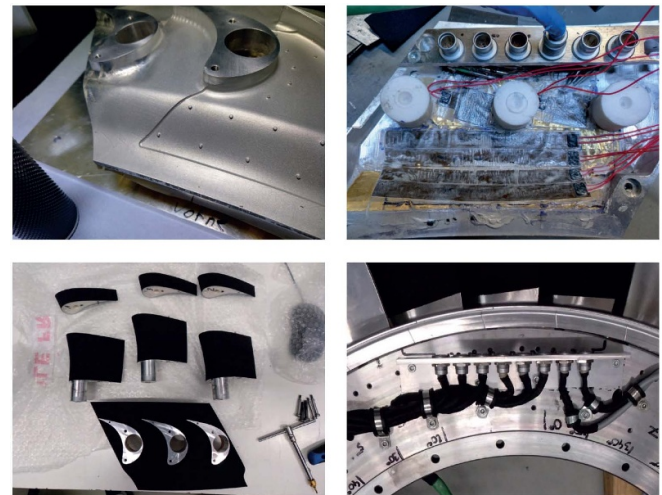

Figure 4. Intermediate steps of instrumentation (top), the ready to install carrier/blade/tip assembly (bottom left) and the integration into the rotor structure (bottom right).

and pixel shift with a major impact on the spatial resolution (blurring) and the resulting signal to noise ratio (SNR). For this study, the integration time is adjusted to 50 μs leading to a pixel shift of less than 13 px. The signal amplitude is expected to be in the range of 700–900 counts for the predefined range of the carrier temperatures. The optical access is realized by a CaF$_2$ window. It is AR-coated, resulting in an average transmissivity of 0.98 in the spectral range of 2.5–4 μm. The window is mounted into a plug in the rotor casing.

The camera is triggered with respect to the AOI. As the preselected integration time of 50 μs has little signal intensity and the accuracy of the results was hard to predict in advance. For this reason, the *multi-integration-time* feature of the camera was used to capture the scene with a second integration time of 100 μs. While capturing a sequence, the integration time is altered between every single frame. The true frame rate is therefore half the rotating frequency of the rotor, that is 8.33 Hz. For the presented measurements, each scene is sampled 1000 times leading to a recording time of 120 s.

The rotating instrumentation and the insulator itself are embedded into an exchangeable measurement inlay. The inlay is replicating three single hub side endwall segments. The insulation layer is realized with a two-component cured resin (EP601 by POLYTEC PT) covering a negative offset of the middle right passage, as illustrated in the 3D CAD image in figure 3. Standard type K mantle thermocouples with a diameter of 0.5 mm are located in circular elevations with internal blind boreholes. They serve as reference points for the *in-situ* camera calibration. T_C, the temperature distribution on the

inner side of the insulator, is measured with another array of thermocouples distributed underneath the insulator. All wiring is realized in a pocket at the inner side of the carrier. Foil heaters are used to control the carrier temperature. They are attached, after the wiring of the thermocouples is finalized. The foils are supplied via ten individual circuits using DC power supply units located in the stationary system. A selection of the thermocouples within the carrier are used to control the heating power.

The structural integration of the measurement inlay is the same as for the single endwall segments. All centrifugal forces are absorbed by the screwed blade bodies. As depicted in figure 4, an array of plug sockets is positioned at the disc ring to allow the connection to the telemetry and slip ring units. The quick coupling system allows a fast and easy exchange of the measurement inlay through the cutout within the rotor casing.

The heating power of the foils is limiting the maximum temperature of the carrier to 338 K. The expected minimum fluid temperature in the relative frame of reference is approximately 5 K lower than the total temperature at the turbine inlet. Hence, meaningful target temperatures of the carrier are in the range of 308 K–338 K. In steps of 5 K seven quasi-isothermal boundary conditions are measured in one series.

The thermal conductivities λ_I and λ_P are considered to be constant for the entire domain and temperature range. The insulation layer thicknesses s_I and s_P are determined with a traversing laser triangulation system equipped with a *Keyence* $^{©}$ *LK-G152* sensor. The specifications and the build-up of the system can be found in Kloss [23]. The carrier is scanned three times; with and without the insulation and with the final painting applied.

2.3. Data processing and data reduction methods

The evaluation algorithm is programmed in Matlab 2019a [24]. All relevant computations are performed on the 640 ×

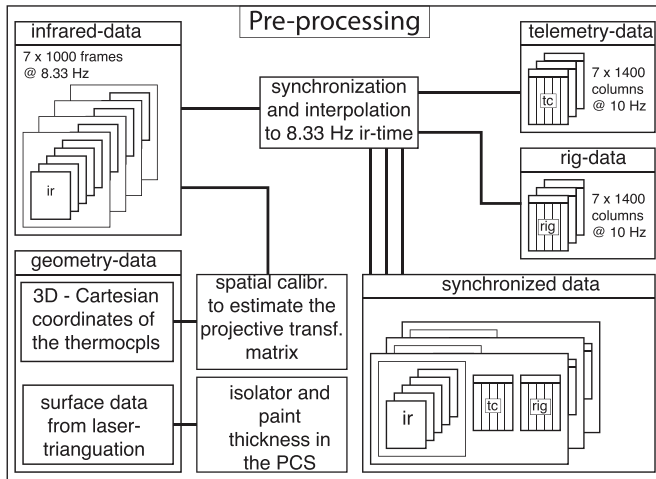**Figure 5.** Structure of the pre-processing procedure.

Figure 6. IR-temperature calibration: 2D surface fits based on thermocouple and the infrared data in respectively on the aluminum elevations.

Figure 7. Procedure to determine h_{ad} and $T_{W,ad}$.

512 pixel coordinate system (PCS). To enable the consideration of covariances between the time series of the infrared and thermocouple signals, the structure and format of the data is crucial regarding storage allocation and computing capacity. As most infrared sequences showed some lost frames, the globally processed number of frames is reduced to 980 leading to a consistent statistical treatment and an appropriate main memory allocation. For each infrared sequence two associated data files are generated. First, the temperatures logged by the telemetry system and the second with all relevant rig-data including temperatures, pressures, mass-flows etc. Both systems are not triggered but sampled continuously with a rate of 10 Hz. They are therefore synchronized and temporally interpolated to the triggered IR-frames. The procedure is depicted in figure 5.

Furthermore, the pre-processing incorporates the allocation and processing of all necessary geometrical information. These are the 3D-coordinates of the thermocouples and the three sets of surface data from the laser-triangulation system. The next step is the estimation of the spatial correlation, i.e. the determination of a valid transformation. As computer vision has made tremendous improvements during the last years, various approaches for camera calibration are available in open literature. The method used here is based on a classical 3D–2D projection scheme with a pinhole projection model. The method to estimate the perspective projection matrix is taken from Distante and Distante [25], section 7.4.2. The aluminum elevations with their high temperature gradients serve as the supporting points in the PCS. The practical realization is presented in section 3.1.

Applying the previously determined transformation matrix to the surface and thermocouple coordinates, they are transformed to the PCS followed by a simple 2D-interpolation scheme. This step is considered noncritical as the surface data is sampled with a higher spatial resolution (four samples per mm) as the PCS.

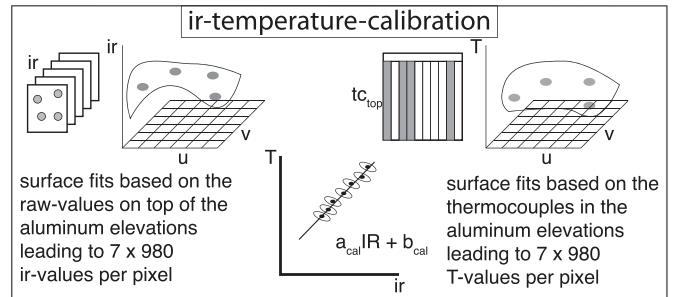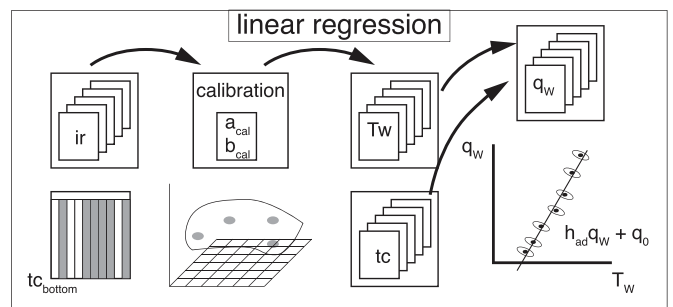For the temperature calibration of the IR-raw signals, the available pairs of raw-signal and temperature information on top of the aluminum elevations are correlated. To quantify the pixel by pixel uncertainties of the calibration coefficients, 2D-surface fits are carried out for every single frame. As presented in section 4 they are essential to estimate the uncertainties in the local specific heat fluxes. The procedure is sketched in figure 6.

Similarly, the temperature distribution on the interface of carrier and insulation again needs to be approximated with the help of discrete temperatures, now using the thermocouples inside the carrier. The approach is equivalent to the surface-fit procedure applied in the calibration process, except the polynomial degrees are increased to three in both coordinates. This is necessary to approximate the actual temperature distribution and does not violate the expected thermal equilibrium in a flat body with a high conductivity. The approach is illustrated in figure 7.

Referencing equation (4), the determination of the local specific heat flux is computed. As indicated above, both temperature distributions are available for every single frame and the associated heat flux can be resolved spatially and for every single frame. For the applied method of fitting the best straight line in the T_W-q_W-plane, this again enables the stochastic description of the sampling points including the covariance between surface temperature and wall heat flux. Equivalent to the calibration process, this is the precondition for a correct statistical evaluation of the derived coefficients, in this case h_{ad}, q_0 and finally $T_{W,ad}$. The detailed description of the statistics and the approximation of the uncertainties is given in section 4.
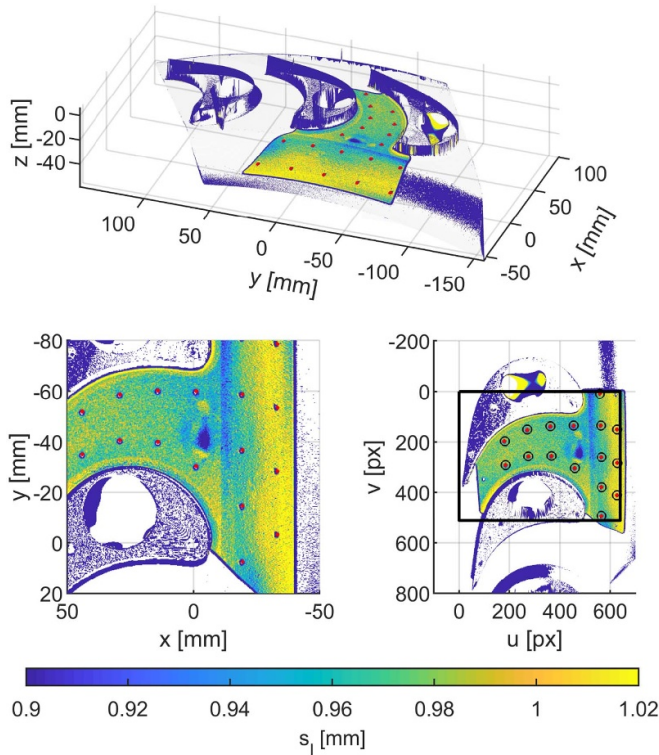
Figure 8. 3D–2D transformation of the insulator thickness s_I. 3D-view based on the local Cartesian coordinate system of the carrier, supplemented by the positions of the reference points (top). The bottom left chart shows the same data but reoriented and enlarged. Applying the determined transformation, the according coordinates in the 2D-PCS are identified and shown in the bottom right view.

3. Results and discussion

3.1. Spatial transformation

The spatial transformation enables the correct allocation of the 3D-based insulator and paint thicknesses as well as the discrete carrier temperatures to their corresponding positions in the PCS. In the top-view of figure 8 the insulator thickness s_I is shown in the 3D-coordinates of the carrier. The data is the result of the pre-processing of the first and second surface scans. The chart is supplemented by the discrete positions of the centers of the aluminum elevations derived from the CAD-file (red bullets). The same data is shown enlarged and reoriented in the bottom-left view. The accordance between CAD and measurement is given.

For the depicted camera view in total 16 reference points are detected and used for the calibration. In the bottom right view of figure 8, the resulting transformation is visualized. The red dots show the transformed CAD-coordinates of the aluminum elevations and the black circles correspond to the reference pixels identified within the infrared image. The error is approximated with the root mean square error between the projected $(u_{i,p}, v_{i,p})$ and originally determined pixel coordinates (u_i, v_i).

$$E_{cam} = \sqrt{\frac{1}{n} \sum_1^n \left[(u_i - u_{i,p})^2 + (v_i - v_{i,p})^2 \right]}. \quad (8)$$

For the data shown in figure 8 this leads to an error of 1.18 px with maximum differences of 1.64 px in u and 1.87 px in v. With the spatial resolution of 5.6 px mm^{-1} the error arising from the calibration is 0.21 mm. This is below the step size of the surface scans of 0.25 mm and is therefore neglected in the quantification of the uncertainties.

3.2. In-situ *calibration*

The calibration process is aimed to correlate the infrared signal to the actual surface temperature distribution. As depicted in Ochs *et al* [26], the measurement situation for internal thermo-fluid flow investigations with infrared thermography increases the number of signal influencing parameters. First, the AOI is observed through an infrared transmitting window, attenuating the signal depending on the window properties. Second, surrounding walls as well as the transmission of the gas itself complicates the aforementioned correlation. For the presented experimental setup the method suggested by Ochs *et al* [26] is considered as inappropriate for two reasons. First, a pre-calibration under the absence of main and secondary flows is not possible for the rotating rotor due to the immediate acceleration within the passage. Second, the scope of the monitored raw-signals is limited to a narrow band. A simple linear fit approach is considered to be more suitable. The correct statistical description of the calibration process is more important than a categorical compliance of the underlying physics.

In fact it is more focused to fully capture the expected temperature span within the AOI to avoid any extrapolation. Hereby, the upper temperature range is not difficult to reach since the reference thermocouples show elevated temperatures compared to the insulated surrounding. The lower end of the calibration band width is represented by the first observed set-point temperature where the heaters are switched off and the temperature difference between aluminum and the outer surface approaches zero.

For the presented results all seven data sets are used in the calibration procedure. As clarified in section 2.3, the available values on the aluminum elevations are used to build the surface-fits and to expand them to the hole PCS. The procedure is shown in figure 9. To give an orientation, the top left image shows the average of the raw sequence of the highest set-point temperature together with the detected reference points. For the two highlighted pixels (1 and 2) the linear fit is shown on the top right chart. The *observed* points are the results of the surface fits. Surface fits are shown for the highest and lowest target temperatures on the left 3D-plots. The depicted spatial resolution is strongly reduced for a better visualization. Both surface fits are supplemented by the distributed reference values.

Furthermore, for the two pixels all seven surface fits are evaluated. They correspond to the data shown in the linear fit chart. Finally, the 2D-distributions of the T_{TC}-intercept a and
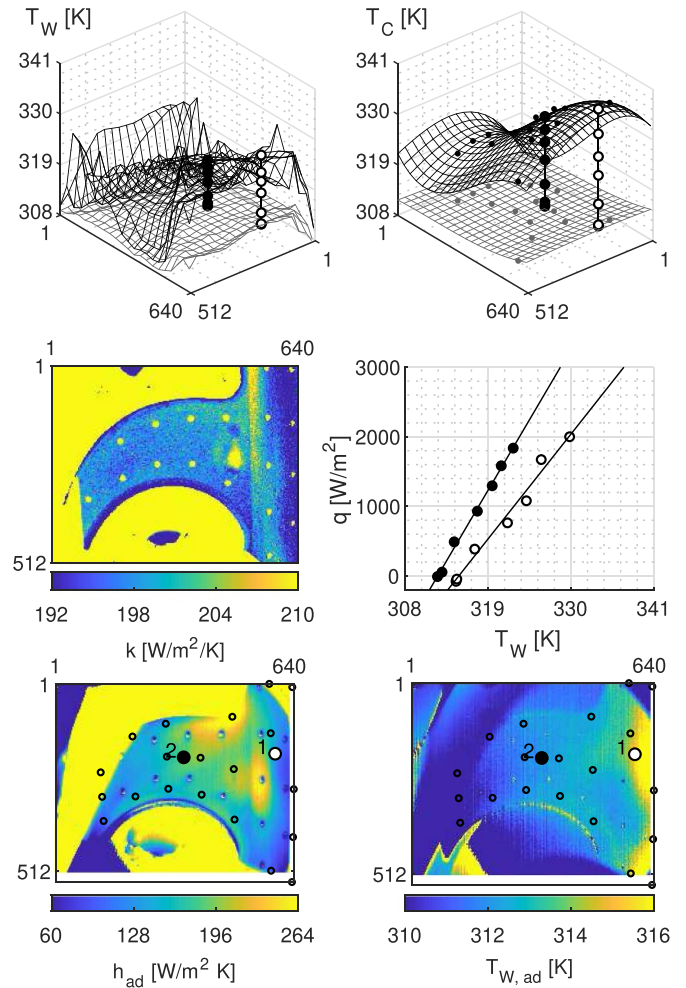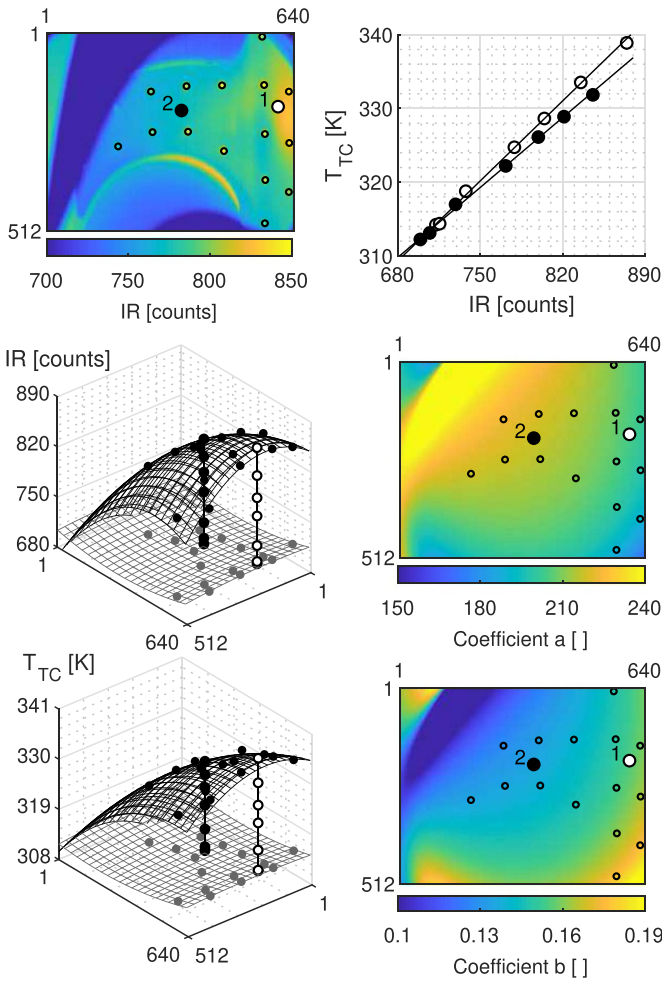
Figure 9. Average of the infrared raw images with detected reference thermocouple positions (top left) and the linear best fit for two exemplary pixels (top right). Surface fits for the approximation of the infrared and temperature distribution of the thermocouples (middle and bottom left). 2D-distribution of the calibration coefficients (middle and bottom right).

Figure 10. The linear fit procedure in the T_W-q_W-plane exemplary presented for two pixels. 2D-distributions of T_W and T_C for the highest and lowest target temperature (top). 2D-distribution of the thermal transmission coefficient k (middle left) and the two straight-line best fit results (middle right). 2D-pixel-based distribution of the two unknows h_{ad} and $T_{W,ad}$ (bottom).

the slope b are shown in the two plots on the right side. Both coefficients are smoothly distributed in the AOI and show an elliptic characteristic with its center in the middle of the frame. The distributions are expected and explainable considering the optical path. For both dominating subsystems, namely the camera lens and the window, the attenuation towards the border areas is increased. The upper left inhomogeneities are physically unlikely. They are originated on high uncertainties due to the narrow temperature range and the missing sampling points in that region.

3.3. Regression analysis and the determination of h_{ad} and $T_{W,ad}$

The calibration coefficients, as shown in the previous section, are available for each pixel and the frame-wise conversion to surface temperatures is straight forward. As stated in section 2.3, the temperature distribution within the carrier is the result of a surface-fit based on the discrete temperature information of the thermocouples distributed underneath the

insulating layer. In the top two charts in figure 10, both approximated 2D temperature distributions are shown for the highest and lowest carrier temperatures. For the carrier, the discrete temperatures are added to visualize exemplary the basis of the surface fits. The polynomial degree is 3 and in each direction of the surface clearly visible for the higher temperature level. The same two pixels as highlighted in the previous section are again selected to illustrate the local linear fit procedure in the T_W-q_W-plane. To recap, each observed point is defined as $q_W = -k(T_W - T_C)$. The 2D-distribution of k is shown in the middle left and the resulting straight-line best fit results on the right. The two highlighted pixels clearly show differences in both coefficients. Position 1 is characterized by a comparatively low adiabatic heat transfer coefficient (slope) but high adiabatic wall temperature ($q_W = 0$). For position 2 that ratio is inverted. The postulated linear dependency obviously holds for both positions. However, the subjective perception of the quality or better the *goodness of fit* is higher for pixel 2.

The application of the linear fit procedure to the entire frame finally leads to a high resolution map of both variables. In the bottom two images in figure 10 the resulting pixel-based distribution of h_{ad} and $T_{W,ad}$ are depicted. The results are not post-processed in terms of a geometrical or smoothing filter. Even if a general interpretation of the underlying thermal-fluid phenomena would be possible within the PCS, the exact geometrical allocation of the results is necessary for a detailed analysis.

3.4. Post-processing—Geometrical filter and interpolation procedure

For the presentation of the heat transfer results, an appropriate geometrical filter and normalization procedure is necessary. First, the corresponding 3D-coordinates of the PCS are determined. The camera calibration process does not yield the full set of intrinsic and extrinsic parameters as the depth information is missing. Anyhow, a work around is applied to achieve a good correspondence for the back-transformation. Therefore, the same interpolation method as carried out to the insulator thickness information may be applied to the Cartesian coordinates itself. After their interpolation on a regular 640×512-uv-grid they are transformed to the global rig-CS with straightforward rotation and translation.

In figure 11 the resulting 3D-view of the heat transfer coefficient together with the surface grid of the entire carrier itself is shown. Furthermore, the hub side edges of the two fillets surrounding the AOI are depicted with the black lines. Now, in this view the exact captured area is easy to interpret and an appropriate geometrical filter may be derived. To reduce unnecessary complexity and for the geometrical normalization, all following steps of the post-processing-procedure are carried out in the ϕ-z-plane of a polar-coordinate-system. The angle is scaled with the mean radius of the hub platform to allow the correct scale in the circumferential direction.

Due to the nonlinear distribution of the discrete pixels a pitch-wise processing, e.g. building the circumferential mean, is not possible in the pixel-based results. To overcome this issue, they are interpolated on a regular ϕ-z-mesh having a slightly lower spatial resolution compared to the original one. Another reason lies in the definition of the geometrical filter. Its application now allows the exact subdivision into single rotor pitches. The resulting 2D-view of the unfiltered data on the regular mesh is shown in the left plot of figure 12. The geometrical filter is indicated with the black lines. Its shape is chosen to just keep data, where a full pitch of valid data is available between the hub side edges of the fillets. The axes are finally normalized by one axial chord-length (including the fillet) in the axial direction and one pitch in the circumference. The origin is located on the leading edge of the left fillet.

Within the areas around the aluminum elevations naturally no linear regression is possible and they also need to be geometrically filtered. As they are surrounded by valid data, an interpolation may be applied to fill them up. A 1D-interpolation scheme in the circumferential direction lead to the best acceptable and continuous gradients. At the end of the
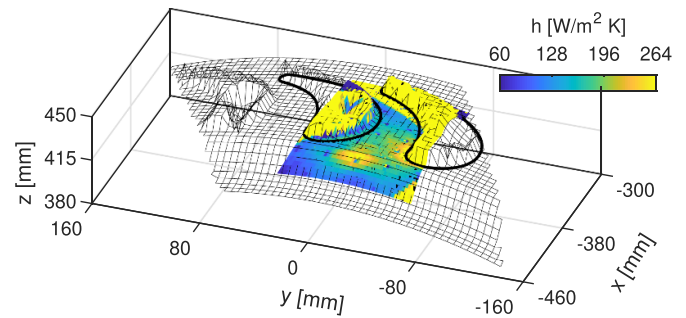

Figure 11. Distribution of the adiabatic heat transfer coefficient h_{ad} transformed back to the 3D-surface of the turbine endwall.
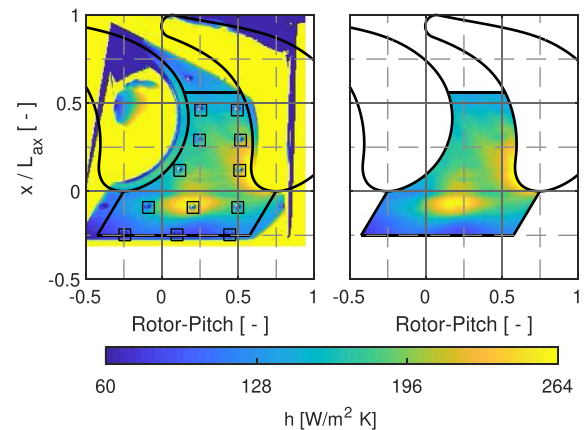

Figure 12. The adiabatic heat transfer coefficient h_{ad} in the normalized ϕ-z-mesh. Geometrically unfiltered, without interpolation of the aluminum elevations and no moving average (left) and fully post-processed (right).

post-processing a moving average of 6 values in the axial direction is applied to smooth out the physically unlikely gradients induced by the noise of the IR-sensor. The post processed result of the heat transfer coefficient is depicted on the right side of figure 12.

3.5. Heat transfer results

The focus of this paper is clearly on the description and evaluation of the measurement method itself. To anyhow introduce the application-oriented capability of the method, a second heat transfer configuration with a rim seal purge flow rate of 2% (of the main flow) is compared to the one presented so far. As thermal design studies often rely on the comparison of different geometries, aero-thermal boundary conditions and test setups in general, dimensionless representatives are suitable to characterize the respective configuration. For the thermal design of turbine components, these are commonly the Nusselt-Number Nu and the film cooling effectiveness η_{ad}.

For both rim seal purge flow rates the 2D-results of Nu and η_{ad} are shown in figure 13. As obvious, qualitative differences in both quantities are clearly visible. As will be shown in the next section, the differences are far above the random part of
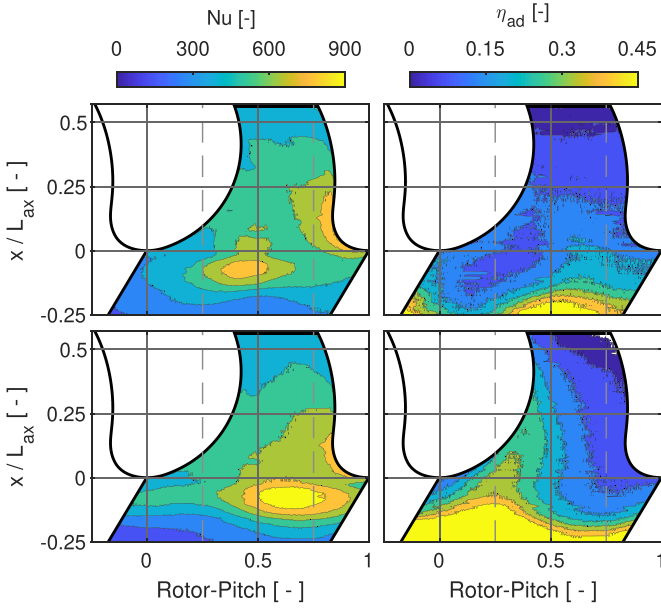
Figure 13. Contour-plots of Nusselt-Number (left) and film cooling effectiveness (right) for two different rim seal purge flow rates (top: 1%–bottom: 2% of the main flow).

Figure 14. 2D-distribution of the relative random part of the combined, experimental uncertainty for h_{ad} and $T_{W,ad}$.

the experimental uncertainties and the quantitative interpretation of delta-examinations is scientifically legitimated.

4. Uncertainties

All definitions and vocabulary, as used in this section, follows the GUM (Guide to the Expression of Uncertainty in Measurement), [27] and the corresponding VIM (International Vocabulary of Metrology), [28]. Concerning the distinction of measurement system uncertainties (random and fixed) to those arising from the so called process unsteadiness, the approach of Moffat [29] is referenced.

The general distinction of either single sample (type A) or multiple sample (type B) based uncertainty analysis is of great importance for the subsequently demonstrated approximation of the overall (combined) uncertainty. As both *true* values of the unknown quantities (h_{ad} and $T_{W,ad}$) are the result of one single regression, they need to be categorized as type B. To remember, the experiment is conducted ones for every operating (measurement) point. However, the observed points in the T_W-q_W-plain are definitely of type A as their estimates and corresponding uncertainties/covariances are the result of, in this case, 980 repeated observations.

On the other hand, the regression-coefficients themselves are indeed the result of multiple observations of the *same* operating point, in this case with 7 *repetitions*. Therefore, the regression method needs to account for both, the statistics of the underlying observed points and their overall influence to the derived coefficients. As traditional linear regression methods based on least-squares estimation (LSE) do not account for uncertainties in both variables (and thus potential covariances too), they are not suitable to properly describe the aforementioned interdependency. Such, for this work a proper
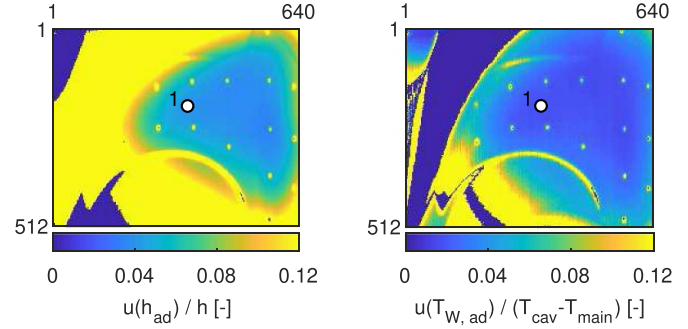
method accounting for (correlated) errors in both variables is applied.

A mathematically well documented procedure is the one published by York [30] in 1968. York has generalized earlier least squares treatments to account for correlations in both variables. In 2004, York *et al* [31] have focused on the unification of the LSE and MLE (maximum likelihood estimation) approaches. Besides, in section III they have rewritten the generalized LSE-equations in a compact and concise form together with the description of an easy to implement iterative algorithm. This approach is implemented twice in the evaluation procedure. First, to derive the calibration coefficients and their uncertainties and second, the linear regression in the T_W-q_W-plain.

To begin with, the result of the uncertainty analysis is shown in the form of 2D-distributions of the relative random part of the combined, experimental uncertainty, see figure 14. The uncertainty of the adiabatic wall temperature is related to the characteristic temperature difference between purge and main flow, $u(T_{W,ad})/(T_{cav} - T_{main})$, as this is the proper temperature span to be resolved in the AOI. As obvious, both relative uncertainties show strong inhomogeneities within the field of interest. The results clearly correspond to the expectation and will be discussed and presented in the following.

Referencing equation (13) and table I in York *et al* [31], the system of equations to be solved iteratively is rewritten. The notation is adapted to the existing problem leading to the following straight line linear equation:

$$q = q_0 + ht; \quad t_{ad} = -\frac{q_0}{h}. \tag{9}$$

The observed points are T_i and Q_i with their weighted averages $\bar{T}$ and $\bar{Q}$. The initial value for h is approximated with simple regression and subsequently allows the calculation of the first q_0:

$$q_0 = \bar{Q} - h\bar{T}; \quad \bar{T} = \frac{\sum W_i T_i}{\sum W_i}; \quad \bar{Q} = \frac{\sum W_i Q_i}{\sum W_i}. \tag{10}$$

The final value of h is then determined iteratively while applying the following expressions for U_i, V_i, W_i and β_i:

$$h = \frac{\sum W_i \beta_i V_i}{\sum W_i \beta_i U_i}; \quad U_i = T_i - \bar{T}; \quad V_i = Q_i - \bar{Q} \tag{11}$$

$$W_i = \frac{\omega(T_i)\omega(Q_i)}{\omega(T_i) + h^2\,\omega(Q_i) - 2\,hr_i\alpha_i} \qquad (12)$$

$$\alpha_i = \sqrt{\omega(T_i)\omega(Q_i)} \qquad (13)$$

$$\beta_i = W_i\left[\frac{U_i}{\omega(Q_i)} + \frac{hV_i}{\omega(T_i)} - (hU_i + V_i)\frac{r_i}{\alpha_i}\right]. \qquad (14)$$

After h has converged, the standard uncertainties of both coefficients $u^2(h)$ and $u^2(q_0)$ as well as their correlation coefficient $r(q_0,h)$ are evaluated, in this case on the basis of the adjusted points $t_i = \bar{T} + \beta_i$ and $q_i = \bar{Q} + h\beta_i$:

$$u^2(h) = \sigma^2(h) = \frac{1}{\sum W_i u_i^2} \qquad (15)$$

$$u^2(q_0) = \sigma^2(q_0) = \frac{1}{\sum W_i} + \bar{t}^2\,\sigma^2(h) \qquad (16)$$

$$r(q_0,h) = -\bar{t}\frac{\sigma(h)}{\sigma(q_0)} \qquad (17)$$

with the definitions for u_i and $\bar{t}$:

$$u_i = t_i - \bar{t} \quad \text{and} \quad \bar{t} = \frac{\sum W_i t_i}{\sum W_i}. \qquad (18)$$

To evaluate the standard uncertainty of the adiabatic wall temperature, the combined uncertainty of h and q_0 must be evaluated at the intercept with the abscissa. Here, the combined uncertainty equals to the uncertainty for predicted q-values (see equation (16) in [27]) leading to the following expressions:

$$q(t) = f(h,q_0) \qquad (19)$$

$$u_c^2(q) = \left(\frac{\partial q}{\partial q_0}\right)^2 u^2(q_0) + \left(\frac{\partial q}{\partial h}\right)^2 u^2(h)$$
$$+ 2\frac{\partial q}{\partial q_0}\frac{\partial q}{\partial h}u(q_0)u(h)r(q_0,h) \qquad (20)$$

$$u_c^2(q) = u^2(q_0) + t^2 u^2(h) + 2\,tu(q_0)u(h)r(q_0,h). \qquad (21)$$

The expression for the uncertainty of the predicted q-value is:

$$q \pm u_c(q) = q_0 + ht \pm u_c(q). \qquad (22)$$

This expression is equated to zero and solved for t:

$$u(t_{\text{ad}}) = \frac{1}{h^2 - u^2(h)}$$
$$\times \left\{\left[u(h)u(q_0)r(q_0,h) - hq_0\right]\right.$$
$$\pm \left[h^2 u^2(q_0) - 2\,hq_0 r(q_0,h)u(h)u(q_0) + q_0^2 u^2(h)\right.$$
$$\left.\left. + r^2(q_0,h)u^2(h)u^2(q_0) - u^2(h)u^2(q_0)\right]^{(1/2)}\right\} \qquad (23)$$

As obvious from equations (12) to (14), the quantification of the individual weights $\omega(T_i)$ and $\omega(Q_i)$ is of primary importance for the uncertainty analysis. A common approach in weighted LSE is to use the reciprocal of the experimental variance. For the expression of type A uncertainties, the variance is derived from the observations themselves and then termed as the experimental standard variance s^2. For a multiple sample analysis, the best estimate for the measured quantity is the arithmetic mean and the experimental standard deviation equals to the square root of its experimental variance ($u(x_i) = s(\bar{X}_i)$ compare 4.2.2 and 4.2.3 in the GUM [27]) leading to:

$$\omega(T_i) = \frac{1}{s^2(\bar{T}_i)} \quad \text{and} \quad \omega(Q_i) = \frac{1}{s^2(\bar{Q}_i)}. \qquad (24)$$

Both variables are based on surface fits and the LSE for the temperature calibration. The *standard* approach, as presented in the GUM, is therefore not suitable for the present study. To account for uncertainties arising from the surface fits and the included LSE, an individual procedure is necessary and established for the presented measurements.

The wall heat flux Q_i is not measured directly but depends on a temperature difference. Its variance therefore must be a combination of the uncertainties in both temperature ratings, taking potential correlations into account. With reference to equation (4), the specific heat flux for each observed target temperature is calculated as:

$$Q_i = k(T_{C,i} - T_{W,i}). \qquad (25)$$

As k is neither assumed to depend on temperature nor it is part of the random uncertainty analysis, the combined uncertainty for Q_i is defined as follows:

$$u_c^2(Q_i) = \left(\frac{\partial Q_i}{\partial T_{C,i}}\right)^2 u^2(T_{C,i}) + \left(\frac{\partial Q_i}{\partial T_{W,i}}\right)^2 u^2(T_{W,i})$$
$$+ 2\frac{\partial Q_i}{\partial T_{C,i}}\frac{\partial Q_i}{\partial T_{W,i}}u(T_{C,i})u(T_{W,i})r(T_{C,i},T_{W,i}). \qquad (26)$$

The evaluation of the partial derivatives finally allows the quantification of the combined uncertainty of Q_i:

$$u_c^2(Q_i) = s^2(\bar{Q}_i)$$
$$= k^2\left[u^2(T_{C,i}) + u^2(T_{W,i})\right.$$
$$\left. - 2u(T_{C,i})u(T_{W,i})r(T_{C,i},T_{W,i})\right]. \qquad (27)$$

To sum up, the weights $\omega(T_i)$ and $\omega(Q_i)$ as well as their correlation coefficient r_i are reduced to expressions containing the experimental uncertainties of the wall temperature $u(T_{W,i})$, the carrier temperature $u(T_{C,i})$ and the two correlation coefficients $r_i = r(Q_i,T_{W,i})$ and $r(T_{C,i},T_{W,i})$.

Each observed point in the T_i-Q_i-plain is evaluated and equations (10)–(14) are iteratively solved. The solution for one single pixel (highlighted in figure 14) is shown in figure 15. All seven observed points are represented by their averages and uncertainty ellipses. The best-fit straight line is depicted
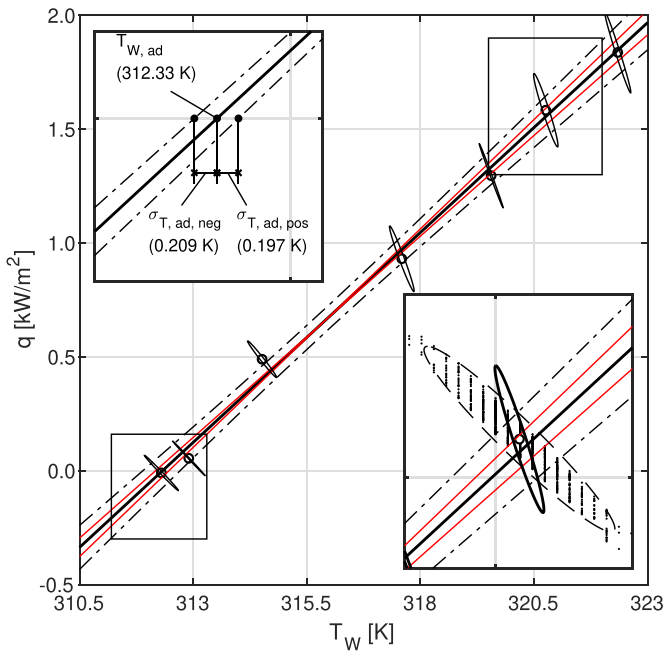
Figure 15. Best-straight line fit procedure for the determination of h_{ad} and $T_{W,ad}$. Ellipses are based on the experimental standard variances and correlation between the wall heat flux and wall temperature. The combined uncertainty for predicted q_W-values allows to determine the uncertainty of the adiabatic wall temperature ($q_W = 0$) enlarged in the top left box with error-bars. For the sixth target temperature, the point-cloud with its uncertainty ellipse is shown (bottom right box).

in solid black, the uncertainty in h_{ad} as the two red lines and the combined uncertainty for predicted q_W values as dash/dot. The evaluation of the uncertainty in T_{ad} is visualized enlarged in the top left box (compare equation (23)).

To sum up, the general look at the best straight line in figure 15 shows that all deviations between the observed and predicted points are all within the uncertainties as they were defined and calculated before. With reference to Moffat [29] the presented overall uncertainty is a first-order uncertainty. The results include the random effects of the measurement system *and* the process unsteadiness, as the available data is recorded while the process is running. A quantification or distinction of the zero-order uncertainty is not possible. Furthermore, up to now, no fixed errors are included in the uncertainty analysis.

5. Conclusion

The presented experimental method is one possible approach to directly determine spatially highly resolved heat transfer quantities on rotating and structurally integrated surfaces. The setup comes together with an enormous effort in the design and manufacturing of the instrumentation as well as the integration into the facility.

One major advantage of the approach however lies in the *in-situ* calibration procedures in both, the spatial and temperature calibration of the camera. The absence of any numerical post processing, as often necessary in iso-energetic

approaches, reduces the experimental uncertainty and allows a direct derivation of the unknowns.

As presented in the uncertainty discussion in section 4, the relative random part of the experimental standard uncertainty is well below 10% for the heat transfer coefficient. For the random part of the adiabatic wall temperature uncertainty, relative to the investigated driving temperature difference, values well below 5% are achievable. In future applications of the approach, their values could potentially be further reduced when the available heating power would be increased. The description of the measurement model, as given in this work, may be used as a basis for an improved *design of experiment*.

Concerning the investigation of 3D-shaped surfaces, the presented setup proved its applicability. As shown for the moderately curved rotor endwall, the data acquisition and their post-processing are mathematically fully described. For stronger curvatures however, the assumption of the wall normal heat flux, the calculation of the isolation thickness and the surface fit procedure to deduce the carrier temperature must be evaluated. Preliminary numerical investigations, especially thermal finite element studies, could be one possible approach to estimate their validity and quantify the associated uncertainties.

Vice versa, for unsophisticated shapes of the investigated surface geometries, the experimental approach would lead to a much simpler design concerning the instrumentation. Where, in contrast to the presented setup, the installation space is less constricted, the integration of more powerful heater elements could be applied. Attention however must be paid to the heat resistance of the applied materials with a focus on the insulating layer and the adhesives for bonding the temperature sensors and electric heater elements. If synthetic materials on the basis of one or two-component adhesives are employed though, the method will be restricted to low temperature environments with target temperatures well below 150 °C. A selection of advanced materials however could lead to high temperature applications of the method. Thermal barrier coatings (TBC), as applied to real engine components, are one possible source of supply. More general speaking, the whole structural integrity together with the instrumentation could follow well established concepts coming from high temperature technical applications.

The presented uncertainty analysis with the statistically based description of the best-fit straight line is suitable for all linear regression approaches in experimental convective heat transfer investigations. Highlighting the fact that most systematic errors can be reduced to a minimum, the presented approach can lead to comparably low absolute measurement uncertainties in the heat transfer quantities.

With reference to figure A1, the frame-based progress of the specific wall heat flux obviously contains fluctuations. This is another major benefit of the post-processing procedure. As instantaneous results are available on the investigated surface, analytical methods are possible in time *and* space. A frequency based evaluation approach can be used to better understand and describe potential non-periodic phenomena, in the present case the postulated influence of *unsteady rim seal flow structures* to the hub side endwall heat transfer.

First attempts to describe the time and space dependent injection of the rim seal purge flow showed great promise. The conducted heat transfer investigations were accompanied by unsteady flow field and wall pressure measurements in the AOI. A rudimentary evaluation of interrelations between observed unsteady pressure fluctuations in the rim seal itself and the time response of the wall heat flux have shown potential correlations. However, the analysis is neither terminated nor verified at the date of publication of this work.

Data availability statement

The data that support the findings of this study are available upon reasonable request from the authors.

Acknowledgments

Appendix. Uncertainties in the temperature measurements

The distribution of the carrier temperature is approximated with a 3×3-surface fit function. The surface fit is carried out individually for every single corresponding frame. For every surface-fit the functional 1σ prediction interval is used to quantify the *goodness of fit*. In the upper chart in figure A1 the 980 evaluated surface-fit functions are shown for the sixth target temperature (black dots, oscillating). The black line depicts the average $\bar{T}_{C,6}$.

The experimental variance of the time series of the fitted carrier temperature is:

$$s^2(T_C) = \frac{1}{n-1} \sum (T_{C,j} - \bar{T}_C) \text{ with } j = 1 : 980. \quad (A.1)$$

The regular type A evaluation of the variance of the mean would be $s^2(\bar{T}_C) = s^2(T_C)/n$. This expression however does not incorporate the uncertain part of the surface-fit-procedure. Therefore, the so called pooled estimate of variance is defined. Here, the single uncertainties s_j^2 are represented by the square of the 1σ prediction intervals.

$$u_p^2(T_C) = s_p^2(\bar{T}_C) = \frac{\sum v_j s_j^2}{\sum v_j} = \frac{\sum v_j \sigma_j^2}{\sum v_j}. \quad (A.2)$$

As each surface fit has the same degree of freedom v_j, the expression is simplified to the unweighted arithmetic mean of the individual variances leading to the total variance of the mean:

$$u^2(T_C) = s^2(\bar{T}_C) = \frac{s^2(\bar{T}_C)}{n} + \frac{\sum s_j^2}{n}. \quad (A.3)$$
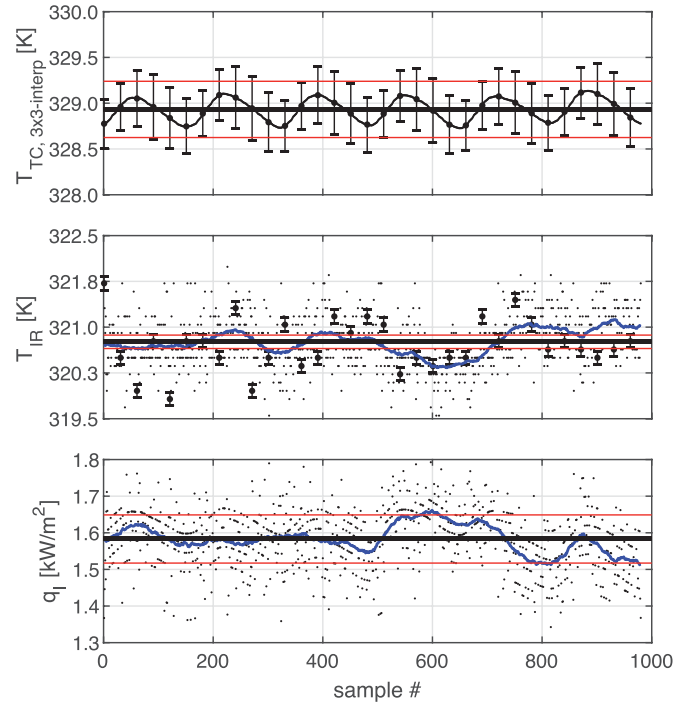

Figure A1. Top: evaluated surface-fit functions based on the carrier temperature thermocouples. Middle: calibrated wall temperatures. Bottom: corresponding wall heat flux. For both temperatures the approximated error-bars are shown for every 30th point. Black straight lines show the averages, the red lines the experimental standard uncertainties of the mean. The blue lines are showing moving averages for wall temperature and wall heat flux to better visualize the negative correlation.

The depicted error-bars in the chart show the standard deviations s_j (just every 30th data point is plotted). The resulting uncertainty of the mean $\bar{T}_C \pm u(\bar{T}_C)$ are indicated by the upper and lower red lines.

As pointed out in section 3.2, the wall temperature is based on the linear-fit determined in the *in-situ* calibration process. Again, Yorks approach is applied to determine the calibration coefficients and their uncertainties.

Exemplary, the 2D average of the calibrated wall temperature of the 6th set-point is shown in figure A2, left. On the right hand side the corresponding uncertainty caused by the calibration procedure is depicted. The evaluation of the uncertainty is again presented for one pixel as marked in the images with the white circle.

Consistently to the approach for the determination of the uncertainty in the carrier temperature distribution, the surface fits over the discrete temperatures in the aluminum elevations $T_{cal,i}$ and their counter parts in the infrared signal $S_{cal,i}$ are statistically evaluated and allow the specification of the single weights and their correlation, compare equation (A.3). Again, for the sixth observed set-temperature, the fitted statistical series of S_{cal} and T_{cal} are shown in figure A3. Error-bars again show the uncertainty arising from the surface fit. The red lines depict the $\bar{T}_{cal,i} \pm u(\bar{T}_{cal,i})$ and $\bar{S}_{cal,i} \pm u(\bar{S}_{cal,i})$.

For the raw signal, the blue line additionally shows a moving average over 60 data points to better visualize the existing
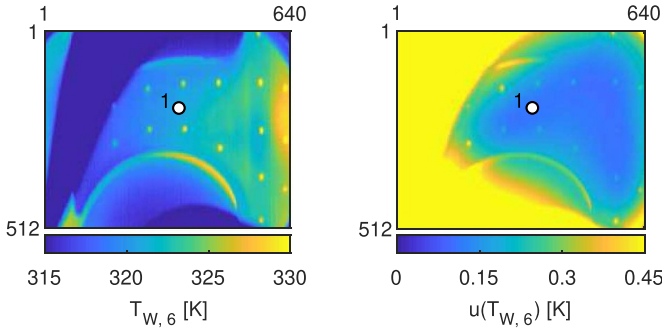
Figure A2. Calibrated wall temperature for the 6th set-point (left) together with the corresponding uncertainty caused by the calibration procedure (right).
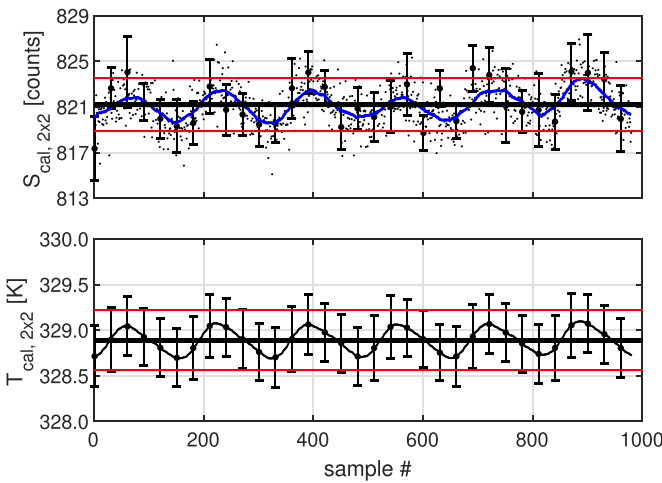

Figure A3. Evaluated surface-fit functions based on the infrared raw signal (Top) and the thermocouples at the reference positions for the *in-situ* calibration.

positive correlation between S_{cal} and T_{cal}. Pearson's correlation coefficient is calculated on the basis of the covariance and standard deviation of the original signals.

$$r(S_{cal,i}, T_{cal,i}) = \frac{\text{cov}(S_{cal,i}, T_{cal,i})}{\sigma(S_{cal,i})\sigma(T_{cal,i})}. \tag{A.4}$$

In figure A4, the local calibration is shown in terms of the fitted best straight line together with the seven observed points. Each point is represented by the averages $\bar{S}_{cal,i}$ and $\bar{T}_{cal,i}$ and an uncertainty ellipses. The shape of the ellipses is based on the standard uncertainties $u(\bar{S}_{cal,i})$ and $u(\bar{T}_{cal,i})$ and their correlation coefficients $r(\bar{S}_{cal,i}, \bar{T}_{cal,i})$. The single data points for the sixth set-point is shown enlarged in the bottom right cutout. The vertices of the ellipses are larger then expected from the underlying point cloud. The ratio of both uncertainties changes the orientation compared to the ellipse based on the covariance matrix of the original two signals.

The fit procedure leads to the two calibration coefficients together with the uncertainties and their correlation. Consistent to equation (21) the combined uncertainty of the
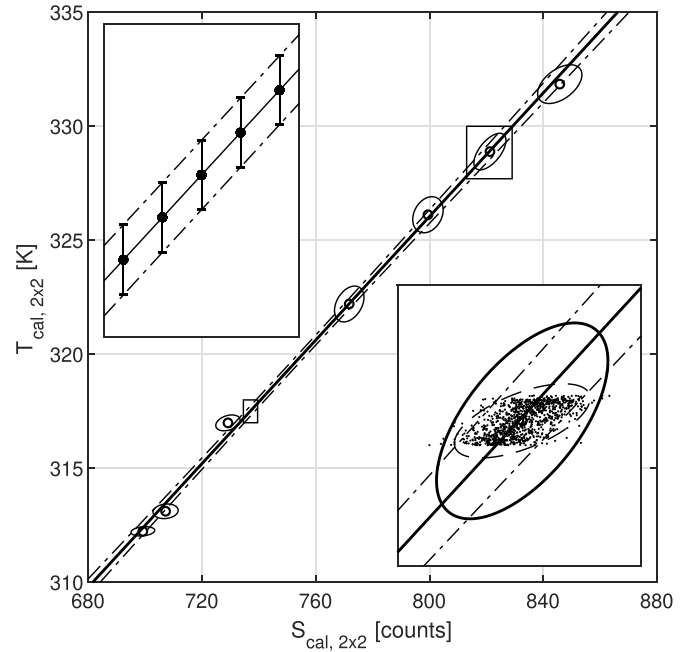

Figure A4. Best-straight line fit procedure for the *in-situ* calibration. Ellipses are based on the experimental standard variances and correlation between raw signal and reference temperatures. The combined uncertainty for the wall temperature is shown enlarged in the top left box with error-bars. For the sixth target temperature, the point-cloud is plotted (bottom right box).

calibration coefficients allows an individual evaluation of the uncertainties for every single infrared image.

The calibrated wall temperatures together with the estimated error-bars (every 30th) are depicted in the middle chart in figure A1. To calculate the resulting variance of the mean the same approach as for the carrier temperature (equation (A.3)) is applied. The result is again shown as the red lines in the plot. The heat flux, its average and its variance finally is calculated with equations (25) and (26) and depicted in the bottom chart in figure A1.

For the sixth target temperature the single data-points are shown enlarged in the bottom right box. They are equivalent to the data shown in figure A1. The two ellipses are based on the same correlation coefficient but different standard deviations. The dashed line is based on the standard deviation of the raw-signals, whereas the solid line uses the experimental measurement uncertainties of the mean. The negative correlation between the wall temperature and the corresponding heat flux is clearly visible. As the wall temperature increases, for example by an instantaneous external flow effect, the difference to the local carrier temperature decreases leading to a lower wall heat flux.

ORCID iDs

T Ostrowski ⓘ https://orcid.org/0000-0001-8699-3688
H-P Schiffer ⓘ https://orcid.org/0000-0002-6499-9154

References

[1] Popović I and Hodson H P 2013 Aerothermal impact of the interaction between hub leakage and mainstream flows in highly-loaded high pressure turbine blades *J. Turbomach.* **135** 61014

[2] Lynch S P and Thole K A 2015 Heat transfer and film cooling on a contoured blade endwall with platform gap leakage *Proc. of the ASME Turbo Expo: Turbine Conf. and Exposition 2015 (New York, N.Y.: ASME)* p V05BT12A037

[3] Laveau B, Abhari R S, Crawford M E and Lutum E 2013 High resolution heat transfer measurement on flat and contoured endwalls in a linear cascade *J. Turbomach.* **135** 41020

[4] Werschnik H, Ostrowski T, Hilgert J, Schneider M and Schiffer H P 2015 Infrared thermography to study endwall cooling and heat transfer in turbine stator vane passages using the auxiliary wall method and comparison to numerical simulations *Quant. InfraRed Thermogr. J.* **12** 1–18

[5] Schuler P 2016 Einfluss der Rotor-Stator-Dichtung auf die Turbinenaerodynamik und Seitenwandkühlung *Dissertation* (temp)

[6] Boudet J, Hills N J and Chew J W 2006 Numerical simulation of the flow interaction between turbine main annulus and disc cavities *Proc. of the ASME Turbo Expo 2006 (New York, NY: ASME)* pp 553–62

[7] Schuepbach P, Abhari R S, Rose M G, Germain T, Raab I and Gier J 2010 Effects of suction and injection purge-flow on the secondary flow structures of a high-work turbine *J. Turbomach.* **132** 21021

[8] Chilla M, Hodson H and Newman D 2013 Unsteady interaction between annulus and turbine rim seal flows *J. Turbomach.* **135** 051024

[9] Beard P F, Gao F, Chana K S and Chew J 2017 Unsteady interaction between annulus and turbine rim seal flows *J. Eng. Gas Turbines Power* **139** 032501

[10] Schädler R, Kalfas A I, Abhari R S, Schmid G and Voelker S 2017 Modulation and radial migration of turbine hub cavity modes by the rim seal purge flow *J. Turbomach.* **139** 011011

[11] Horwood J T M, Hualca F P, Wilson M, Scobie J A, Sangan C M and Lock G D 2018 Unsteady computation of ingress through turbine rim seals *ASME Turbo Expo 2018: Turbomachinery Conf. and Exposition*

[12] Hualca F P, Horwood J T M, Sangan C M, Lock G D and Scobie J A 2020 The effect of vanes and blades on ingress in gas turbines *J. Eng. Gas Turbines Power* **142**

[13] Abhari R S, Guenette G R, Epstein A H and Giles M B 1992 Comparison of time-resolved turbine rotor blade heat transfer measurements and numerical calculations *J. Turbomach.* **114** 818–27

[14] Blair M F 1994 An experimental study heat transfer in a large-scale turbine rotor passage *J. Turbomach.* **116** 1–13

[15] Laveau B, Abhari R S, Crawford M E and Lutum E 2015 High resolution heat transfer measurements on the stator endwall of an axial turbine *J. Turbomach.* **137** 41005

[16] Lazzi Gazzini S, Schädler R, Kalfas A I and Abhari R S 2017 Infrared thermography with non-uniform heat flux boundary conditions on the rotor endwall of an axial turbine *Meas. Sci. Technol.* **28** 025901

[17] Gazzini S L, Schädler R, Kalfas A I, Abhari R S, Hohenstein S, Schmid G and Lutum E 2017 Effect of purge air on rotor endwall heat transfer of an axial turbine *Proc. of the 1st Global Power and Propulsion Forum* vol GPPF-2017-95

[18] Hänni D D, Abhari R S, Schädler R, Kalfas A I, Schmid G, Lutum E and Lecoq N 2019 Purge flow effects on rotor hub endwall heat transfer with extended endwallcontouring into the disk cavity *Global Power and Propulsion Zurich19: Conf.* (GPPS) GPPS Zurich19

[19] Werschnik H, Hilgert J, Wilhelm M, Bruschewski M and Schiffer H P 2017 Influence of combustor swirl on endwall heat transfer and film cooling effectiveness at the large scale turbine rig *J. Turbomach.* **139** 081007

[20] Moffat R J 1998 What's new in convective heat transfer? *Int. J. Heat Fluid Flow* **19** 90–101

[21] Gritsch M, Baldauf S, Martiny M, Schulz A and Wittig S 1999 The superposition approach to local heat transfer coefficients in high density ratio film cooling flows *ASME 1999 Int. Gas Turbine and Aeroengine Congress and Exhibition* p V003T01A048

[22] Eitenmüller J, Wilhelm M, Gresser L, Ostrowksi T, Leichtfuss S, Schiffer H P, Lyko C and Naik S 2019 Highly accurate delta efficiency measurements at the large scale turbine rig *Proc. of the ASME Turbo Expo (New York, N.Y.: The American Society of Mechanical Engineers)*

[23] Kloss M 2015 Stoffübergang in durchströmten, rotierenden Relativsystemen Aussagefähigkeit der Naphthalin-Sublimations-Methode *Dissertation* Universitäts- und Landesbibliothek Darmstadt, Darmstadt

[24] MATLAB 2019 *Version 9.6.0 (R2019a)* (Natick, MA: The MathWorks Inc.)

[25] Distante A and Distante C 2020 *Handbook of Image Processing and Computer Vision: Volume 3: From Pattern to Object* 1st ed (Springer)

[26] Ochs M, Horbach T, Schulz A, Koch R and Bauer H J 2009 A novel calibration method for an infrared thermography system applied to heat transfer experiments *Meas. Sci. Technol.* **20** 075103

[27] ISO-IEC Guide 2008 *Guide to the Expression of Uncertainty Measurement (GUM: 1995): Guide Pour l'Expression de l'Incertitude de Mesure (GUM: 1995) (ISO-IEC Guide)* vol 98-3 1st ed (Geneva: Int. Organisation of Standardization)

[28] 2012 *Int. vocabulary of metrology - basic and general concepts and associated terms (vim): Vocabulaire international de métrologie—concepts fondamentaux et généraux et termes associés (vim)*

[29] Moffat R J 1988 Describing the uncertainties in experimental results *Exp. Thermal Fluid Sci.* **1** 3–17

[30] York D 1968 Least squares fitting of a straight line with correlated errors *Earth Planet. Sci. Lett.* **5** 320–4

[31] York D, Evensen N M, Martínez M L and de Basabe Delgado J 2004 Unified equations for the slope, intercept, and standard errors of the best straight line *Am. J. Phys.* **72** 367–75